

A dynamic subgrid-scale model for compressible turbulence and scalar transport

P. Moin, K. Squires, W. Cabot, and S. Lee

Citation: [Physics of Fluids A: Fluid Dynamics](#) **3**, 2746 (1991); doi: 10.1063/1.858164

View online: <https://doi.org/10.1063/1.858164>

View Table of Contents: <http://aip.scitation.org/toc/pfa/3/11>

Published by the [American Institute of Physics](#)

Articles you may be interested in

[A dynamic subgrid-scale eddy viscosity model](#)

[Physics of Fluids A: Fluid Dynamics](#) **3**, 1760 (1991); 10.1063/1.857955

[A proposed modification of the Germano subgrid-scale closure method](#)

[Physics of Fluids A: Fluid Dynamics](#) **4**, 633 (1992); 10.1063/1.858280

[Statistical theory for compressible turbulent shear flows, with the application to subgrid modeling](#)

[The Physics of Fluids](#) **29**, 2152 (1986); 10.1063/1.865552

[Direct numerical simulation of turbulent channel flow up to \$Re_\tau=590\$](#)

[Physics of Fluids](#) **11**, 943 (1999); 10.1063/1.869966

[An eddy-viscosity subgrid-scale model for turbulent shear flow: Algebraic theory and applications](#)

[Physics of Fluids](#) **16**, 3670 (2004); 10.1063/1.1785131

[A dynamic model for subgrid-scale variance and dissipation rate of a conserved scalar](#)

[Physics of Fluids](#) **10**, 3041 (1998); 10.1063/1.869832

A dynamic subgrid-scale model for compressible turbulence and scalar transport

P. Moin, K. Squires, W. Cabot, and S. Lee

Center for Turbulence Research, Stanford University, Stanford, California 94305 and NASA/Ames Research Center, Moffett Field, California 94035

(Received 1 April 1991; accepted 15 July 1991)

The dynamic subgrid-scale (SGS) model of Germano *et al.* [Phys. Fluids A 3, 1760 (1991)] is generalized for the large eddy simulation (LES) of compressible flows and transport of a scalar. The model was applied to the LES of decaying isotropic turbulence, and the results are in excellent agreement with experimental data and direct numerical simulations. The expression for the SGS turbulent Prandtl number was evaluated using direct numerical simulation (DNS) data in isotropic turbulence, homogeneous shear flow, and turbulent channel flow. The qualitative behavior of the model for turbulent Prandtl number and its dependence on molecular Prandtl number, direction of scalar gradient, and distance from the wall are in accordance with the total turbulent Prandtl number from the DNS data.

I. INTRODUCTION

In large eddy simulation (LES) the large-scale field is computed directly from the solution of the filtered (local volume-averaged) Navier–Stokes equations, and the small-scale stresses are modeled. The subgrid-scale (SGS) model then represents the effect of the small scales on the large-scale motions. The severe Reynolds number restriction in direct numerical simulation (DNS) is largely alleviated in LES. This advantage is obtained at the expense of modeling the small scales. However, since the small scales are presumably more isotropic and more universal in character for different flows than the large scales, it should be possible to parametrize the small scales using simpler and more universal models.

Relatively little effort has been devoted to SGS modeling despite its purported importance as an alternative to single-point closures for solving engineering problems. The Smagorinsky¹ model remains as the most widely used model in large eddy simulations. The limitations of the Smagorinsky model (or its variants) are the following:

- (i) The optimal model constant must be changed in different flows;
- (ii) the model does not have the correct limiting behavior near the wall;
- (iii) the model does not vanish in laminar flow, and it is demonstrated to be too dissipative in the laminar/turbulent transition region;
- (iv) the model does not account for backscatter of energy from small scales to large scales, which has been shown to be of importance in the transition regime;
- (v) compressibility effects are not included in the model.

Several modifications to the Smagorinsky model have been proposed to account for mean-flow complexities, but they are generally based on *ad hoc* foundations. Improvements have also been sought in analogy with single-point closure models by using moment equations for the SGS stresses.^{2,3}

The key element that has been lacking in most SGS modeling efforts has been the effective utilization of the

large-scale field which is computed directly. This rather rich spectral information is not available in methods based on Reynolds-averaged equations and should be brought to bear in large eddy simulations. The model of Bardina *et al.*⁴ is a rare example where an attempt is made to extrapolate from the computed large-scale field to model the small scales; however, this model still relies on a supplementary Smagorinsky model to provide the necessary SGS dissipation. Several improved SGS models have been developed in Fourier space based on statistical theories of homogeneous turbulence.⁵ Although they are appealing because of their more rigorous theoretical foundations, these models are of little use for inhomogeneous flows, where the problems are formulated in physical space and where accurate SGS models are really needed.

Recently, Germano *et al.*⁶ developed a new SGS model that appears to have overcome many of the aforementioned deficiencies. They used the scale-similarity ideas of Bardina *et al.*⁴ and Germano⁷ to derive an eddy viscosity model. The model uses the strain rate fields at two different scales and thus utilizes spectral information in the large-scale field to extrapolate the small-scale stresses. Using an algebraic identity derived by Germano⁷ and using an eddy viscosity model to represent the SGS stresses at both scales, an expression for the eddy viscosity coefficient was derived which is a function of space and time. The coefficient can be negative in some regions and thus does not totally exclude backscatter, it provides for the proper asymptotic behavior of the stresses near the wall without *ad hoc* damping functions, and it vanishes in laminar flow without *ad hoc* intermittency functions. Large eddy simulations of the transitional and turbulent channel flows using this model were very encouraging. Specifically, the agreements with the DNS results were as good or better than those obtained with variants of the Smagorinsky model but without the fine-tuning and the *ad hoc* components that such models have required.

The main objective of this paper is to extend the dynamic model ideas to the LES of compressible flows and scalar transport. Erlebacher *et al.*⁸ performed a LES of compressible isotropic turbulence. They generalized the Smagorinsky

and scale-similarity model of Bardina *et al.* to include the compressibility effects and energy transport. They used their DNS data to obtain the eddy viscosity model constant. However, as also pointed out by Erlebacher *et al.*, the model constant cannot be obtained uniquely. Since the model is a tensor and varies in space, it can only be obtained in some average sense. For example, the constant obtained using the so-called rms and least-square methods differed by about a factor of 2. It is also likely that the constant would be different had they used the DNS data at a different Reynolds number or at a different instant in time. In some of the early large eddy simulations of isotropic decay⁹ the value of the Smagorinsky constant was determined by matching the computational decay rate of turbulent kinetic energy to experimental data.¹⁰

Another objective of this study was to perform a LES of the decay of isotropic turbulence using the dynamic model. In the dynamic model, the model coefficient is determined **instantaneously during the calculations rather than being specified *a priori***. It was therefore of great interest to determine whether the dynamic model can predict the energetics of isotropic turbulence without additional input—i.e., to determine whether the same model that was highly successful in the LES of turbulent and transitional channel flow can predict the energy decay rate in isotropic turbulence, which has been the key turbulent flow for calibrating phenomenological turbulence models. The governing equations and the derivation of the dynamic SGS model for compressible flows are given in Sec. II. The model parameters evaluated using DNS data are presented in Sec. III; the DNS data from isotropic turbulence, homogeneous shear flow, and incompressible turbulent channel flow with passive scalars were used. The results from large eddy simulations of essentially incompressible and compressible isotropic turbulence and comparisons with the experimental data are presented in Sec. IV.

II. MATHEMATICAL FORMULATION

In this section the formalisms of Germano *et al.*⁶ for the dynamic SGS model for incompressible flows are extended to compressible flows. We begin with the derivation of the governing equations for the large-scale field. Consider the momentum, continuity, and temperature (internal energy) equations:

$$\begin{aligned} \frac{\partial \rho}{\partial t} + \frac{\partial}{\partial x_k} (\rho v_k) &= 0, \\ \frac{\partial \rho v_k}{\partial t} + \frac{\partial}{\partial x_l} (\rho v_k v_l) &= -\frac{\partial p}{\partial x_k} + \frac{\partial \sigma_{kl}}{\partial x_l}, \\ \frac{\partial C_v \rho T}{\partial t} + \frac{\partial}{\partial x_k} (C_v \rho v_k T) &= -p \frac{\partial v_k}{\partial x_k} + \sigma_{ik} \frac{\partial v_k}{\partial x_i} \\ &\quad + \frac{\partial}{\partial x_k} \left(\kappa \frac{\partial T}{\partial x_k} \right), \end{aligned} \quad (1)$$

where

$$\sigma_{kl} = -\frac{2}{3} \mu \frac{\partial v_j}{\partial x_j} \delta_{kl} + \mu \left(\frac{\partial v_k}{\partial x_l} + \frac{\partial v_l}{\partial x_k} \right), \quad (2)$$

ρ is the density, v_k is the velocity component in the k th direction, p is the pressure, T is the temperature, and C_v is the **specific heat at constant volume**, which will be assumed to be constant. Here κ is the thermal conductivity, and μ is the molecular viscosity which has a power-law dependence on temperature of $\mu/\mu_0 = (T/T_0)^{0.76}$; the molecular Prandtl number ($\text{Pr} \equiv C_p \mu / \kappa$, where C_p is the **specific heat at constant pressure**) is kept constant at 0.7.

Let a filtered or large-scale flow quantity be denoted by an overbar:

$$\bar{f} = \int_D G(\mathbf{x} - \mathbf{x}') f(\mathbf{x}') d\mathbf{x}', \quad (3)$$

where G is some spatial filter and the integral is over the flow domain. Different filter functions have been considered in large eddy simulations. In this paper we use the sharp cutoff filter in wave space, which is conveniently defined in Fourier space by

$$\mathcal{G}_i(k_i) = \begin{cases} 1, & \text{if } k_i \leq \pi/\Delta_i; \\ 0, & \text{otherwise;} \end{cases}$$

where \mathcal{G}_i is the Fourier coefficient of the filter function in the i th direction and Δ_i is the respective filter width. Applying the spatial filter G to the governing equations leads to

$$\begin{aligned} \frac{\partial \bar{\rho}}{\partial t} + \frac{\partial}{\partial x_k} (\bar{\rho} \bar{v}_k) &= 0, \\ \frac{\partial}{\partial t} \bar{\rho} \bar{v}_k + \frac{\partial}{\partial x_l} (\bar{\rho} \bar{v}_k \bar{v}_l) &= -\frac{\partial \bar{p}}{\partial x_k} + \frac{\partial \bar{\sigma}_{kl}}{\partial x_l}, \\ C_v \frac{\partial \bar{\rho} \bar{T}}{\partial t} + C_v \frac{\partial}{\partial x_k} (\bar{\rho} \bar{v}_k \bar{T}) &= -\bar{p} \frac{\partial \bar{v}_k}{\partial x_k} + \sigma_{ik} \frac{\partial \bar{v}_k}{\partial x_i} \\ &\quad + \frac{\partial}{\partial x_k} \left(\kappa \frac{\partial \bar{T}}{\partial x_k} \right). \end{aligned} \quad (4)$$

The large-scale field equations are operationally simpler when the variables are recast in terms of Favre-filtered quantities. A Favre-filtered (or density-weighted) variable is defined as

$$\tilde{f} = \bar{\rho} f / \bar{\rho}. \quad (5)$$

Note that

$$\bar{\rho} \bar{v}_k = \bar{\rho} \tilde{v}_k, \quad \bar{\rho} \bar{v}_k \bar{v}_l = \bar{\rho} \tilde{v}_k \tilde{v}_l, \quad \text{and} \quad \bar{\rho} \bar{v}_k \bar{T} = \bar{\rho} \tilde{v}_k \tilde{T}.$$

We will use the following decomposition of the stress tensor and the heat flux, respectively, into resolved and SGS components:

$$\begin{aligned} \bar{\rho} \tilde{v}_k \tilde{v}_l &= \bar{\rho} \tilde{v}_k \tilde{v}_l + \underbrace{\bar{\rho} (\tilde{v}_k \tilde{v}_l - \tilde{v}_k \tilde{v}_l)}_{\tau_{kl}}, \\ \bar{\rho} \tilde{v}_k \tilde{T} &= \bar{\rho} \tilde{v}_k \tilde{T} + \underbrace{\bar{\rho} (\tilde{v}_k \tilde{T} - \tilde{v}_k \tilde{T})}_{q_k}. \end{aligned}$$

The filtered ideal gas equation of state is

$$\bar{p} = R \bar{\rho} \bar{T} = \bar{\rho} R \tilde{T}. \quad (6)$$

Models will be presented in Sec. III for the SGS stress tensor τ_{kl} and the heat flux vector q_k . There are several other

terms that need special treatment. These are the viscous terms in the momentum and energy equations, and the pressure-dilatation and conduction terms in the energy equation. In the treatment of these terms, we will make essentially the same approximations as were made by Erlebacher *et al.*⁸ This is consistent with objectives of this study, that is to derive and test extensions of the dynamic model for the SGS stresses and heat flux and to compare the results with those using the standard models. Consider the pressure-dilatation term: Using the equation of state, we have

$$\begin{aligned} p \frac{\partial v_k}{\partial x_k} &= \rho R T \frac{\partial v_k}{\partial x_k} = \bar{\rho} R T \frac{\partial v_k}{\partial x_k} \\ &= \bar{\rho} R \tilde{T} \frac{\partial \tilde{v}_k}{\partial x_k} + \bar{\rho} R \left[T \frac{\partial v_k}{\partial x_k} - \tilde{T} \frac{\partial \tilde{v}_k}{\partial x_k} \right]. \end{aligned}$$

The small-scale contributions in the square brackets are neglected. It is argued that the fluctuation Mach number for the small scales is small and therefore the dilatation of the small scales is negligible. Using low Reynolds number DNS data of isotropic turbulence at several Mach numbers, the neglected term was found to be at most 5% of SGS heat flux. However, in some cases, it was comparable to the other retained terms. Similar approximations were made for the other terms where their small-scale components were neglected. Thus, the governing equations for the large-scale field are

$$\begin{aligned} \frac{\partial \bar{p}}{\partial t} + \frac{\partial}{\partial x_k} \bar{\rho} \tilde{v}_k &= 0, \\ \frac{\partial \bar{\rho} \tilde{v}_k}{\partial t} + \frac{\partial}{\partial x_l} (\bar{\rho} \tilde{v}_k \tilde{v}_l) &= - \frac{\partial \bar{p}}{\partial x_k} + \frac{\partial}{\partial x_l} \tilde{\sigma}_{kl} - \frac{\partial}{\partial x_l} \tau_{kl}, \quad (7) \\ C_v \frac{\partial \bar{\rho} \tilde{T}}{\partial t} + C_v \frac{\partial}{\partial x_k} (\bar{\rho} \tilde{v}_k \tilde{T}) \\ &= - \bar{p} \frac{\partial \tilde{v}_k}{\partial x_k} + \tilde{\sigma}_{ik} \frac{\partial \tilde{v}_k}{\partial x_l} \\ &\quad + \frac{\partial}{\partial x_k} \left(\tilde{\kappa} \frac{\partial \tilde{T}}{\partial x_k} \right) - C_v \frac{\partial q_k}{\partial x_k}, \end{aligned}$$

where $\tilde{\sigma}_{kl}$ and $\tilde{\kappa}$ are the same as σ_{kl} in (2) and κ except that all constituent variables are replaced with their Favre-filtered counterparts.

A. Subgrid-scale model for the momentum equations

To close the momentum equations, τ_{kl} must be modeled. Using (5), τ_{kl} is recast in terms of spatially filtered variables:

$$\begin{aligned} \tau_{kl} &= \bar{\rho} (\tilde{v}_k \tilde{v}_l - \tilde{v}_k \tilde{v}_l) \\ &= \overline{\rho v_k v_l} - (\overline{\rho v_k} \overline{\rho v_l} / \bar{\rho}). \end{aligned}$$

The key element of the dynamic model concept is the utilization of the spectral data contained in the resolved field. This information is brought to bear by introducing a "test filter" with a larger filter width than the resolved grid filter, which generates a second field with scales larger than the resolved field. Let a spatially test-filtered quantity be denoted by a caret. The width of the test filter is denoted by Δ . The test-

filtered stresses \mathcal{T}_{kl} are defined by direct analogy to SGS stresses τ_{kl} :

$$\mathcal{T}_{kl} = \overline{\rho v_k v_l} - (\overline{\rho v_k} \overline{\rho v_l} / \hat{\rho}).$$

Note that the test filter is always applied to the resolved field (denoted by an overbar). Thus, quantities with $\hat{\cdot}$ are filtered (or smoothed) flow variables obtained from the computed field.

Using Germano's⁷ identity, the Leonard stresses⁹ \mathcal{L}_{kl} can be expressed in terms of \mathcal{T}_{kl} and τ_{kl} :

$$\begin{aligned} \mathcal{L}_{kl} &\equiv \mathcal{T}_{kl} - \hat{\tau}_{kl} = \left(\overline{\frac{\rho v_k \rho v_l}{\bar{\rho}}} \right) - \frac{\overline{\rho v_k} \overline{\rho v_l}}{\hat{\bar{\rho}}} \\ &= \overline{(\bar{\rho} \tilde{v}_k \tilde{v}_l)} - \frac{1}{\hat{\bar{\rho}}} (\hat{\bar{\rho} \tilde{v}_k} \hat{\bar{\rho} \tilde{v}_l}). \quad (8) \end{aligned}$$

The right-hand side is completely computable from the resolved variables.

We use the trace-free Smagorinsky eddy viscosity model⁸ for τ_{kl} . However, as will be shown below in the development of the dynamic model, the eddy viscosity coefficient will be computed and is a function of instantaneous flow variables. Let

$$\tau_{kl} - \frac{1}{3} q^2 \delta_{kl} = -2C \bar{\rho} \Delta^2 |\tilde{S}| (\tilde{S}_{kl} - \frac{1}{3} \tilde{S}_{mm} \delta_{kl}), \quad (9)$$

where $q^2 = \tau_{ii}$ is the isotropic part of the SGS Reynolds stress tensor, $\tilde{S}_{kl} = \frac{1}{2} (\partial \tilde{u}_k / \partial x_l + \partial \tilde{u}_l / \partial x_k)$, and $|\tilde{S}| = (2\tilde{S}_{kl}\tilde{S}_{kl})^{1/2}$. In the incompressible limit, this model reduces to the Smagorinsky model. In contrast to incompressible flows, where q^2 is absorbed into the pressure, it must be modeled for compressible flows. The SGS energy q^2 is parametrized using Yoshizawa's^{8,11} expression:

$$q^2 = 2C_I \bar{\rho} \Delta^2 |\tilde{S}|^2. \quad (10)$$

Erlebacher *et al.*⁸ neglected q^2 on the grounds that it is negligible compared to the thermodynamic pressure. This approximation will be discussed later in this paper.

We will use Eq. (8) to compute the coefficients C and C_I . To determine C_I , the trace of Eq. (8) is used in conjunction with the model of Eq. (10) for \mathcal{T}_{kk} and τ_{kk} :

$$\begin{aligned} \overline{\hat{\rho} \tilde{v}_k \tilde{v}_k} - (1/\hat{\bar{\rho}}) (\hat{\bar{\rho} \tilde{v}_k}) (\hat{\bar{\rho} \tilde{v}_k}) \\ = 2C_I (\hat{\bar{\rho} \Delta^2 |\tilde{S}|^2} - \Delta^2 \bar{\rho} |\tilde{S}|^2). \quad (11) \end{aligned}$$

Although Eq. (11) can be used to solve for C_I , which would be a function of space and time, Germano *et al.*,⁶ using *a priori* tests, showed that an expression similar to that multiplying C_I on the rhs of (11) can become zero at some grid points. Therefore, an averaging procedure on relations like (11) was needed to make the determination of C_I and the other SGS coefficients well conditioned. It will be assumed that C_I is independent of the directions in which the flow is homogeneous. Thus, for temporally developing homogeneous flows, C_I is considered to be only a function of time. Volume averaging of (11) leads to

$$C_I = \frac{\langle \overline{\hat{\rho} \tilde{v}_k \tilde{v}_k} - (1/\hat{\bar{\rho}}) (\hat{\bar{\rho} \tilde{v}_k}) (\hat{\bar{\rho} \tilde{v}_k}) \rangle}{\langle 2\hat{\bar{\rho} \Delta^2 |\tilde{S}|^2} - 2\Delta^2 \bar{\rho} |\tilde{S}|^2 \rangle}, \quad (12)$$

where $\langle \rangle$ indicates volume averaging. For channel flow, which is also considered in this paper, C_I is considered to be a function of the distance from the walls and of time, and $\langle \rangle$

indicates averaging over planes parallel to the walls. In complex inhomogeneous flows more localized space and time averages should be used. Finally, the model for q^2 is

$$q^2 = \frac{\overline{\rho \langle \widehat{\rho \tilde{v}_k \tilde{v}_k} - (1/\hat{\rho}) (\widehat{\rho \tilde{v}_k}) (\widehat{\rho \tilde{v}_k}) \rangle}}{\langle (\hat{\Delta}/\Delta)^2 \hat{\rho} |\tilde{S}|^2 - \overline{\rho |\tilde{S}|^2} \rangle} |\tilde{S}|^2. \quad (13)$$

To obtain C , we also use the model (9) for the test field stresses:

$$\mathcal{T}_{kl} - \frac{1}{3} \mathcal{T}_{mm} \delta_{kl} = -2C \hat{\rho} \hat{\Delta}^2 |\tilde{S}| (\hat{S}_{kl} - \frac{1}{3} \hat{S}_{mm} \delta_{kl}). \quad (14)$$

$$C = \frac{\langle [\widehat{\rho \tilde{v}_k \tilde{v}_l} - (1/\hat{\rho}) (\widehat{\rho \tilde{v}_k}) (\widehat{\rho \tilde{v}_l})] \tilde{S}_{kl} - \frac{1}{3} \hat{S}_{mm} (\mathcal{T}_{jj} - \hat{\tau}_{jj}) \rangle}{\langle -2\hat{\rho} \hat{\Delta}^2 |\tilde{S}| (\hat{S}_{kl} \tilde{S}_{kl} - \frac{1}{3} \hat{S}_{mm} \tilde{S}_{jj}) + 2\Delta^2 (\overline{\rho |\tilde{S}|} \tilde{S}_{kl} \tilde{S}_{kl} - \frac{1}{3} \overline{\rho |\tilde{S}|} \hat{S}_{mm} \tilde{S}_{jj}) \rangle}, \quad (15)$$

where

$$\mathcal{T}_{jj} - \hat{\tau}_{jj} = \mathcal{L}_{jj} = \widehat{\rho \tilde{v}_j \tilde{v}_j} - (1/\hat{\rho}) (\widehat{\rho \tilde{v}_j}) (\widehat{\rho \tilde{v}_j}).$$

When C is used in Eq. (9), the only adjustable input to the model will be the ratio of the two filter widths, $\alpha = \hat{\Delta}/\Delta$, which also appears in Eq. (13). Equation (15) reduces to that derived by Germano *et al.*⁶ for constant density incompressible flow. In the LES calculations reported here, α was chosen to be 2 (cf. Ref. 6). Germano *et al.* found the computed turbulence statistics to be insensitive to this ratio. In Sec. IV we will also examine the sensitivity of LES results to this parameter. A different expression for C would be obtained if a different tensor was contracted with the identity (8). However, the specific choice of this tensor is not expected to significantly alter the results of LES since it would appear both in the numerator and denominator of (15). LES calculations using two very different contracting tensors led to less than a 10% change in some turbulence statistics. Another issue that is currently being addressed is the requirement for spatial averaging in Eqs. (13) and (15) which appears to be a problem for numerical analysis rather than turbulence modeling.

B. Subgrid-scale model for the energy equation

To close the energy equation, q_k must be modeled. Using (5), q_k is recast in terms of spatially filtered variables:

$$q_k = \overline{\rho v_k T} - (1/\bar{\rho}) \overline{\rho v_k} \bar{\rho T}.$$

Consider the eddy diffusivity SGS model

$$q_k = -\frac{\bar{\rho} \nu_T}{Pr_t} \frac{\partial \bar{T}}{\partial x_k}, \quad (16)$$

where $\nu_T = C\Delta^2 |\tilde{S}|$ is the eddy viscosity model with C defined in (15), and Pr_t is the SGS turbulent Prandtl number to be determined using the dynamic model.

Let Q_k denote the heat flux at the test filter scale:

$$Q_k = \widehat{\rho v_k T} - (1/\hat{\rho}) \widehat{\rho v_k} \widehat{\rho T}.$$

At the test filter level the same eddy diffusivity model is used:

$$Q_k = -\frac{C \hat{\rho} \hat{\Delta}^2 |\tilde{S}|}{Pr_t} \frac{\partial \hat{T}}{\partial x_k}. \quad (17)$$

Let

Using (9) and (14) in (8), we obtain

$$\begin{aligned} \widehat{\rho \tilde{v}_k \tilde{v}_l} - (1/\hat{\rho}) (\widehat{\rho \tilde{v}_k}) (\widehat{\rho \tilde{v}_l}) \\ = \frac{1}{3} \mathcal{T}_{mm} \delta_{kl} - 2C \hat{\rho} \hat{\Delta}^2 |\tilde{S}| (\hat{S}_{kl} - \frac{1}{3} \hat{S}_{mm} \delta_{kl}) \\ - \frac{1}{3} \hat{\tau}_{mm} \delta_{kl} + 2C \Delta^2 \bar{\rho} |\tilde{S}| (\tilde{S}_{kl} - \frac{1}{3} \tilde{S}_{mm} \delta_{kl}). \end{aligned}$$

To solve for C , we contract this expression with \tilde{S}_{kl} (cf. Ref. 6) and, after the appropriate spatial averaging, we obtain

$$\begin{aligned} \mathcal{K}_k = Q_k - \hat{q}_k &= \overline{(1/\bar{\rho}) \overline{\rho v_k} \bar{\rho T}} - (1/\bar{\rho}) \overline{\rho v_k} \bar{\rho T} \\ &= \widehat{\rho \tilde{v}_k T} - (1/\hat{\rho}) \widehat{\rho \tilde{v}_k} \widehat{\rho T}, \end{aligned} \quad (18)$$

which is directly computable. To compute the turbulent Prandtl number Pr_t , we substitute (16) and (17) into (18):

$$\begin{aligned} \widehat{\rho \tilde{v}_k T} - \frac{1}{\hat{\rho}} \widehat{\rho \tilde{v}_k} \widehat{\rho T} \\ = -\frac{C}{Pr_t} \left(\hat{\rho} \hat{\Delta}^2 |\tilde{S}| \frac{\partial \hat{T}}{\partial x_k} - \Delta^2 \bar{\rho} |\tilde{S}| \frac{\partial \bar{T}}{\partial x_k} \right). \end{aligned}$$

Contracting with $\partial \hat{T} / \partial x_k$ and performing the appropriate spatial averaging, we obtain

$$\begin{aligned} Pr_t = C \left\langle \hat{\Delta}^2 \hat{\rho} |\tilde{S}| \frac{\partial \hat{T}}{\partial x_k} \frac{\partial \bar{T}}{\partial x_k} - \Delta^2 \bar{\rho} |\tilde{S}| \frac{\partial \bar{T}}{\partial x_k} \frac{\partial \bar{T}}{\partial x_k} \right\rangle \\ \times \left\langle \left(\frac{1}{\hat{\rho}} \widehat{\rho \tilde{v}_k} \widehat{\rho T} - \widehat{\rho \tilde{v}_k T} \right) \frac{\partial \bar{T}}{\partial x_k} \right\rangle^{-1}, \end{aligned} \quad (19)$$

where C is given by (15). For constant density flows, ρ drops out and this expression for the SGS turbulent Prandtl number can be used for the transport of a passive scalar in incompressible flows.

III. EVALUATION OF THE MODEL COEFFICIENTS USING DIRECT NUMERICAL SIMULATION DATA

Direct numerical simulation data were used to evaluate the expressions for the model constants and turbulent Prandtl number in compressible isotropic turbulence, homogeneous shear flow, and turbulent channel flow. The simulation velocity and temperature fields were filtered and test filtered for this purpose.

A. Isotropic turbulence

A priori determination of the model coefficients was performed using several of the DNS flow fields computed by Lee *et al.*¹² These flow fields were obtained from the numerical solution of the compressible Navier–Stokes equations (1) in a periodic box. Spatial derivatives were computed by finite-difference methods which possess spectral-like resolution as well as sixth-order formal accuracy. The difference

equations were time advanced using a third-order accurate Runge-Kutta method. The same numerical method was used in the large eddy simulations reported in Sec. IV. Two cases with different initial temperature and pressure fluctuations were considered. The pseudoincompressible fields (case 1) were obtained from direct numerical simulations in which the initial field was solenoidal, and the initial pressure fluctuations were obtained from the solution of the incompressible Poisson equation; the density was uniform and the initial temperature field was obtained from the equation of state and, thus, had an initial spectrum similar to the pressure. The flow fields for case 2 were generated using zero initial pressure and temperature fluctuations. Therefore, the temperature field developed solely from the compressibility effects. The equilibrium fields from these latter computations contained eddy shocklets, i.e., small-scale regions of large compression. For each simulation the initial density was uniform and the initial velocity field for each case was divergence free and constructed from an energy spectrum of the form

$$E(k) \sim k^4 \exp[-2(k/k_p)^2].$$

The value of k_p , the wave number corresponding to the peak in the energy spectrum, for all of the simulation results presented in this section was 4 (for a computational box of length 2π). The value of the microscale Reynolds number Re_λ in the initial field was 35.1 for both cases and the initial turbulence Mach number M_i was 0.519.

The DNS computations were performed on a 64^3 grid ($k_{\max} = 32$) (note that $N/2$ complex Fourier modes are sufficient to describe a real function of one space dimension defined on N grid points). To evaluate the SGS coefficients a Fourier cutoff filter was applied at $k_i = 16$ and the test-filter cutoff was at $\hat{k}_i = 8$ (i.e., $\alpha = 2$). The filter width used for evaluation of constants was defined as $(\Delta_1 \Delta_2 \Delta_3)^{1/3}$, where Δ_i is the filter width in the i th direction. The dynamic SGS stress coefficients and turbulent Prandtl numbers from both cases are shown in Fig. 1. The time axis in these figures has been made dimensionless using the eddy turnover time, $\tau_t = \lambda/u'$, in the initial field. Here, λ is the Taylor microscale, and u' is the rms streamwise turbulence intensity. As can be seen from the figure, there is relatively little influence of the shape of the initial temperature spectrum on the SGS stress coefficients, though both C and C_t are slightly lower for case 2 (uniform initial temperature). The values of C shown in Fig. 1(a) vary between roughly 0.008 and 0.014. In most of the evolution time, these values are larger than the value of $C = 0.0085$ determined by Erlebacher *et al.*,⁸ though it should be noted that a value of 0.016 was also determined in their study using a different statistical measure. Our definition of $|S|$ in Eq. (9) is larger than that in Ref. 8 by a factor of $\sqrt{2}$. Thus, for consistency with our definition we have divided the values reported in Ref. 8 by this factor. In addition, it should be noted that the square root of C corresponds to the definition of the Smagorinsky constant C_s . The values of C_t shown in Fig. 1(a) range between approximately 0.0025 and 0.009. In their study, Erlebacher *et al.* neglected the isotropic part of the SGS stresses (equivalent to $C_t = 0$) since *a priori* tests conducted in their study

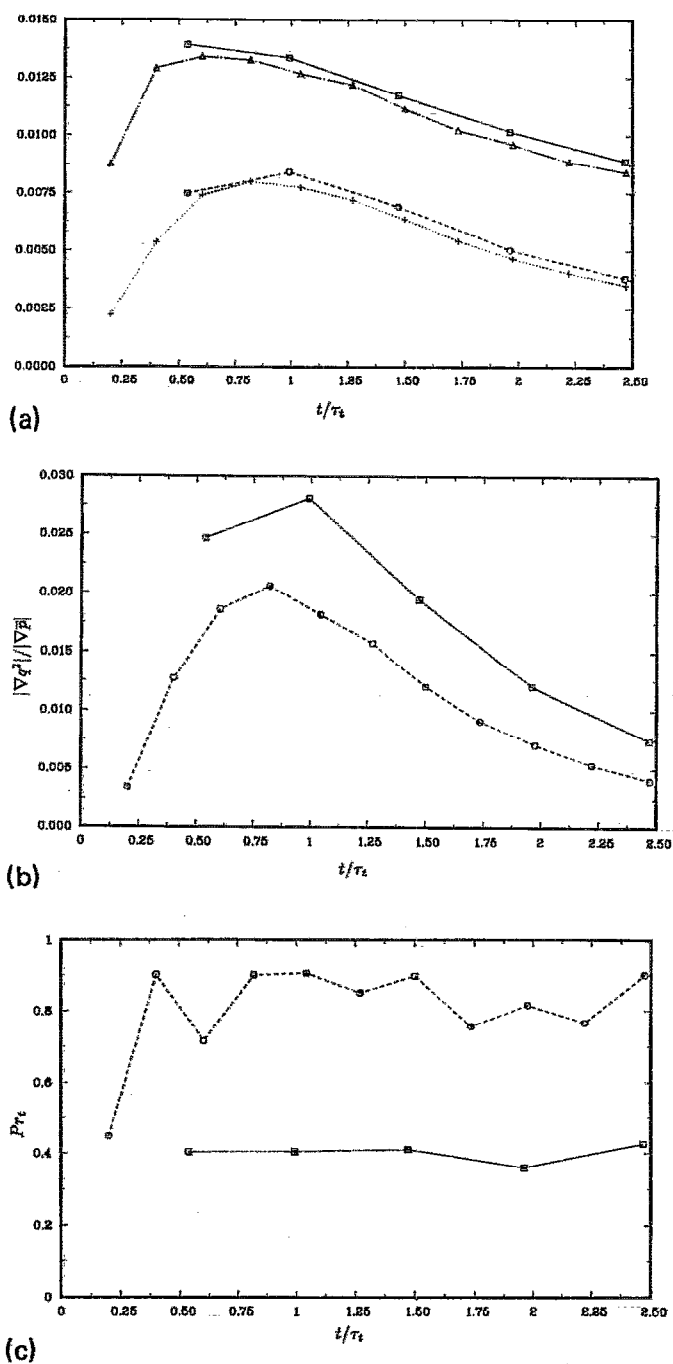


FIG. 1. (a) Time development of model coefficients from *a priori* tests of compressible isotropic turbulence (from 64^3 DNS). \square — \square , C (case 1); \circ — \circ , C_t (case 1); \triangle — \triangle , C (case 2); $+$ \cdots $+$, C_t (case 2). (b) Root mean square ratio of subgrid-scale energy gradient to pressure gradient from *a priori* tests of compressible isotropic turbulence. \square — \square , case 1; \circ — \circ , case 2. (c) Time development of turbulent Prandtl number from *a priori* tests of compressible isotropic turbulence. \square — \square , case 1; \circ — \circ , case 2.

using DNS data showed this term to be small relative to the thermodynamic pressure. Shown in Fig. 1(b) is the ratio of the magnitudes of the SGS kinetic energy gradient to the gradient of the thermodynamic pressure for cases 1 and 2. Consistent with the results of Erlebacher *et al.*, this ratio is indeed observed to be small exhibiting a peak value of less

than 3%. We emphasize, however, that results from *a priori* tests using DNS fields at low Reynolds numbers may not necessarily extrapolate to the results obtained from LES typically performed at a much higher Reynolds number (see Sec. IV).

The time development of Pr_t from the *a priori* tests of cases 1 and 2 is shown in Fig. 1(c). There is a significant effect of the initial temperature spectrum on the turbulent Prandtl number. The value of Pr_t predicted by the dynamic model for case 1 is nearly constant around 0.4, which is near the optimal value used in Refs. 8 and 13. The value of Pr_t from case 2 is approximately 0.85. Higher values of turbulent Prandtl number should not necessarily be attributed to the compressibility effects; it may simply be a manifestation of different initial temperature fluctuation spectra relative to the velocity fluctuations. In any case, these results point to a possible deficiency of models with fixed constants that are independent of the instantaneous flow conditions. In fact, our LES computations reported in Sec. IV reveal that the model coefficients depend on several factors such as initial energy spectrum, grid resolution, and the removal of aliasing errors. Since all such factors influence the transfer of energy from large scales to small scales, we expect that they should also influence the model coefficients.

The model coefficients shown in Figs. 2(a) and 2(b) were obtained from *a priori* tests of DNS fields computed using 128^3 grid points ($k_{\max} = 64$) and further illustrate the effect of factors such as grid resolution and energy spectrum on the model coefficients. In order to evaluate the model coefficients, a Fourier cutoff filter was applied at $k_i = 32$ and the test-filter cutoff was at $\hat{k}_i = 16$ ($\alpha = 2$). Note that the values of C and C_T in Fig. 2(a) are significantly smaller than those shown in Fig. 1(a). The value of Re_λ in the initial field was 50 and the initial value of M_i was 0.61. For the 128^3 simulations the initial temperature and pressure fields were uniform.

B. Incompressible homogeneous shear flow

Extensive DNS data of Rogers *et al.*¹⁴ were used to evaluate the dynamic model coefficients. Since these computations were incompressible with passive scalars, only C and Pr_t were evaluated. The computations of Rogers *et al.* were performed on a 128^3 grid ($k_{\max} = 64$). They considered two reference Reynolds numbers Re of 50 and 100 (corresponding to initial microscale Reynolds numbers Re_λ of 26 and 52, respectively), three molecular Prandtl numbers ($Pr = 0.2, 0.7$, and 2.0), and three mutually orthogonal directions of mean scalar gradients with a uniform mean shear rate $S = \partial U / \partial y$. We have used all of these flow fields to assess the dependence of the model coefficients on the flow parameters. In addition, two grid resolutions were used to study the dependence of the model coefficients on computational parameters in large eddy simulations, and to observe the trends and applicability of the model in the limit of very coarse-grid LES (i.e., for second-order closures). Fine- and coarse-mesh-filtered fields were obtained using cutoff wave numbers $k_i = 32$ and 16, respectively, and the test-filtered fields for both cases were obtained using cutoff wave

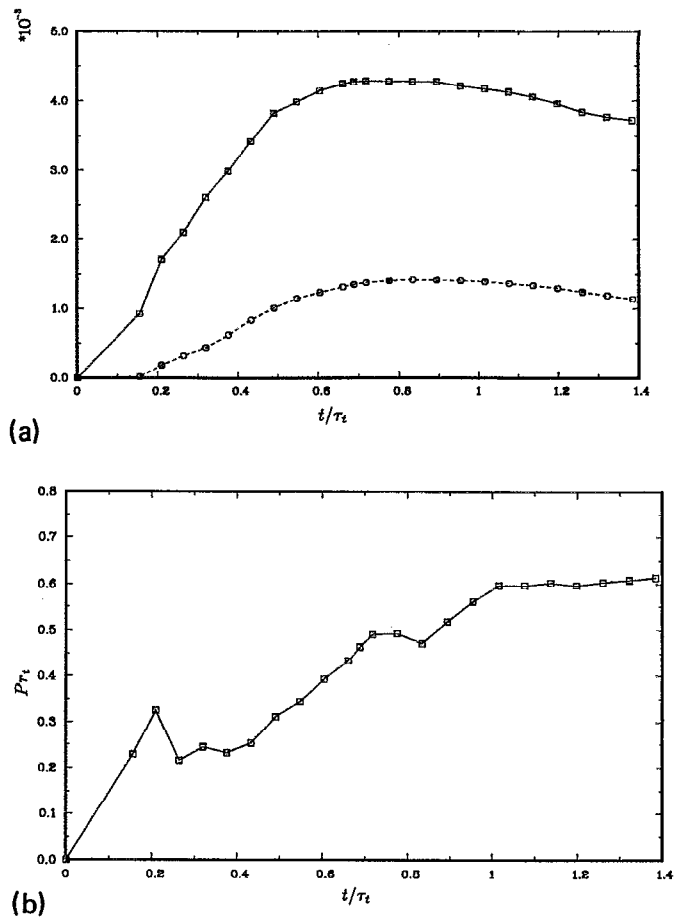


FIG. 2. (a) Time development of model coefficients from *a priori* tests of compressible isotropic turbulence (from 128^3 DNS). \square — \square , C ; \circ — \circ , C_T . (b) Time development of turbulent Prandtl number from *a priori* tests of compressible isotropic turbulence.

numbers half as large as those for the respective filtered fields (i.e., keeping $\alpha = 2$).

The variation of C with time is shown in Fig. 3 for the two Reynolds numbers and for the coarse- and fine-mesh grids. In the fine-mesh case, C appears to be independent of Reynolds number in the early part of the flow evolution. For both Reynolds numbers, C increases significantly later in the flow evolution. Notice that C is larger using the coarse-mesh data. Also note that the dependence of C on the grid is significantly reduced at the higher Reynolds number.

Rogers *et al.*¹⁴ calculated the total turbulent Prandtl number

$$Pr_T \equiv \frac{\langle uv \rangle (\partial T / \partial x_i)}{\langle \theta u_i \rangle (\partial U / \partial y)}, \quad (20)$$

where $u_i = (u, v, w)$ are the fluctuating velocity components, and T and θ are the mean and fluctuating scalar (temperature). Rogers *et al.*¹⁴ demonstrated significant variation of Pr_T with time, molecular Prandtl number Pr , and the direction of the scalar gradient. The dependence of the SGS turbulent Prandtl number Pr_t on the direction of the scalar gradient for different values of Pr is shown in Fig. 4. These dependencies show a remarkable agreement in qualitative behavior with Pr_T calculated from the DNS data of Rogers

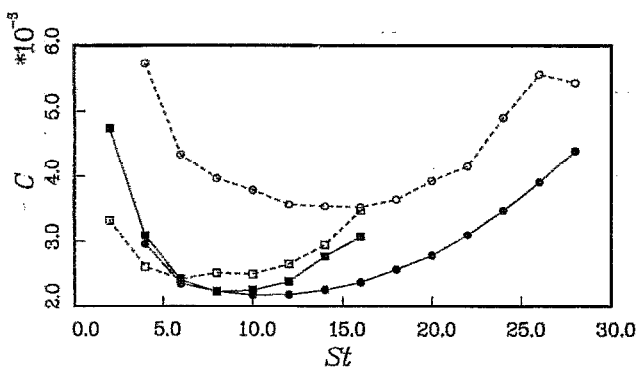


FIG. 3. Time development of model coefficients from *a priori* tests of homogeneous shear flow.¹⁴ \circ , $Re = 50$ and \square , $Re = 100$; filled and open symbols are results from the fine and coarse grids, respectively, with $\alpha = 2$.

et al. For example, Pr_t exhibits the same hierarchy of values for different directions of the mean scalar gradient as Pr_T : values are largest for the mean scalar gradient aligned with the mean shear in the normal (y) direction and lowest for the mean scalar gradient aligned with the mean velocity in the streamwise (x) direction. In Fig. 5, Pr_t for three molecular Prandtl numbers and for two different grids are shown for the case with mean scalar gradient aligned with the mean shear. Of particular interest are the higher values of Pr_t found with the coarser grid, which approach the total turbulent Prandtl number values of 0.8–0.9 computed by Rogers *et al.* Note that for a very coarse LES grid the subgrid-scale

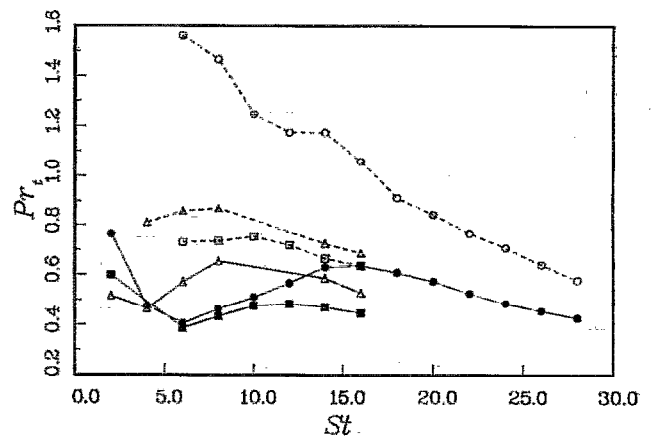


FIG. 5. Time development of model turbulent Prandtl numbers from *a priori* tests of homogeneous shear flow¹⁴ for a passive scalar with gradient in the normal direction. Δ , $Pr = 0.2$; \square , $Pr = 0.7$; and \circ , $Pr = 2.0$; filled and open symbols are results from the fine and coarse grids, respectively, with $\alpha = 2$.

model is expected to account for most of the turbulent transport. The tendency of values of Pr_t to move toward those of Pr_T with the coarser grid was also observed with the other alignments of the mean scalar gradient.

We expect there to be a close correspondence between Pr_t from (19) and Pr_T from (20) provided that the mean shear and scalar gradient dominate the total strain-rate tensor and scalar gradient, and that the domain of wave space sampled in expressions (15) and (19) (which comprises a subset of wave numbers $< \hat{k}_t$) will contain a significant amount of turbulent intensity to characterize the total Reynolds shear stress and scalar flux in (20). The latter condition is more likely to hold for the coarser grids, and the above results appear to support this expectation.

C. Subgrid-scale turbulent Prandtl number in channel flow

Germano *et al.*⁶ evaluated the SGS stress coefficient C in incompressible turbulent channel flow using the DNS data of Kim *et al.*¹⁵ Here, we use the DNS channel data of Kim and Moin¹⁶ with passive scalar (temperature) fields. The flow and the scalar fields were statistically stationary. The channel walls were kept at different uniform temperatures. The Reynolds number based on the centerline velocity and channel half-width was 3300, and three molecular Prandtl numbers ($Pr = 0.1, 0.71$, and 2.0) were considered. The simulations were performed using a $128 \times 129 \times 128$ mesh in the streamwise (x), vertical (y), and spanwise (z) directions, respectively, corresponding to $k_{\max} = 64$ in the x and z directions. The velocity and scalar fields were filtered only in planes parallel to the walls. Again, two computational grids were considered: fine-mesh fields with grid filter cutoff wave numbers $k_x = k_z = 32$ and coarse-mesh fields with $k_x = k_z = 16$. Test-filter cutoff wave numbers were chosen to be half of the respective grid filter wave numbers ($\alpha = 2$). For this case, the angle brackets in Eqs. (15) and (19) denote averages over planes parallel to the walls.

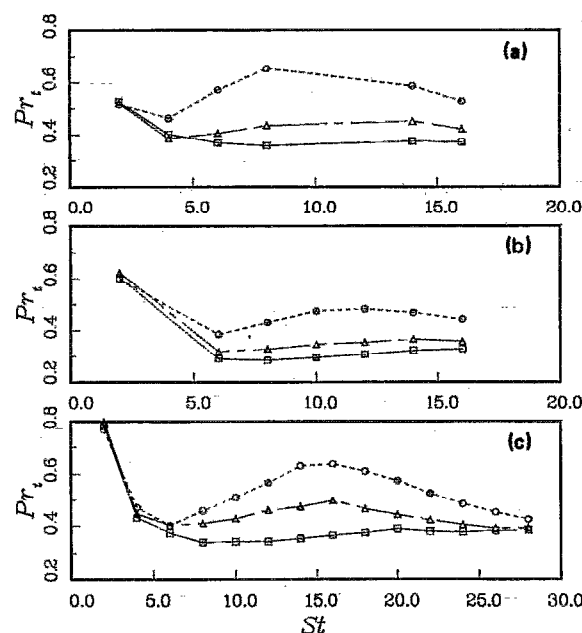


FIG. 4. Time development of model turbulent Prandtl numbers from *a priori* tests of homogeneous shear flow¹⁴ for passive scalars with molecular Prandtl number Pr of (a) 0.2, (b) 0.7, and (c) 2.0 computed on the fine grid with $\alpha = 2$. Scalar gradients are in \square , streamwise; \circ , normal; and Δ , spanwise directions.

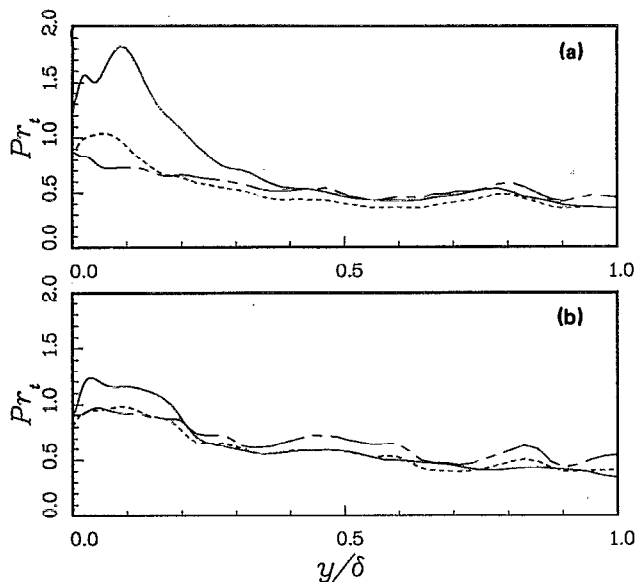


FIG. 6. Model turbulent Prandtl numbers for passive scalars from *a priori* tests of channel flow¹⁶ as functions of distance from the wall y in units of channel half-width δ computed with $\alpha = 2$ on (a) the fine grid and (b) the coarse grid. —, $Pr = 0.1$; ---, $Pr = 0.71$; and - · -, $Pr = 2.0$.

Turbulent Prandtl numbers Pr_t as a function of the distance from the wall are shown in Fig. 6(a). Near the wall, for $Pr = 0.1$, Pr_t peaks and is significantly higher than those for the higher molecular Prandtl numbers. This behavior was also reported¹⁶ for the total turbulent Prandtl number. Near the centerline, values of Pr_t for all three cases are about 0.5, which is not far from the values obtained in isotropic turbulence [case 1, Fig. 1(c)] and homogeneous shear flow (Fig. 4). For the total turbulent Prandtl number Pr_T , Kim and Moin¹⁶ reported values of 1.0 (for $Pr = 0.1$) and 0.75 (for $Pr = 0.71$ and 2.0) near the centerline. Turbulent Prandtl number profiles for the coarse-mesh fields are shown in Fig. 6(b). Their centerline values are only slightly higher than those for the fine-mesh fields in Fig. 6(a), rising much less toward the centerline values of Pr_T than in the homogeneous shear flow cases (cf. Fig. 5). The most significant change in the results from fine- to coarse-mesh filtering seen in Fig. 6 is the large reduction of Pr_t for $Pr = 0.1$ near the wall.

IV. LARGE EDDY SIMULATION OF ISOTROPIC TURBULENCE

To determine the accuracy of the dynamic SGS model, it was used in the LES of nearly incompressible and compressible isotropic turbulence using the same numerical method¹² described in Sec. III A. The incompressible version of the model has been successfully tested in turbulent and transitional channel flows.⁶ As was pointed out in the Introduction, the isotropic decay problem has been used in the past to determine the model constants for the best fit to the experimental and DNS data.

A. Incompressible simulations

For the nearly incompressible simulations, experimental data of Comte-Bellot and Corrsin¹⁰ were used to assess

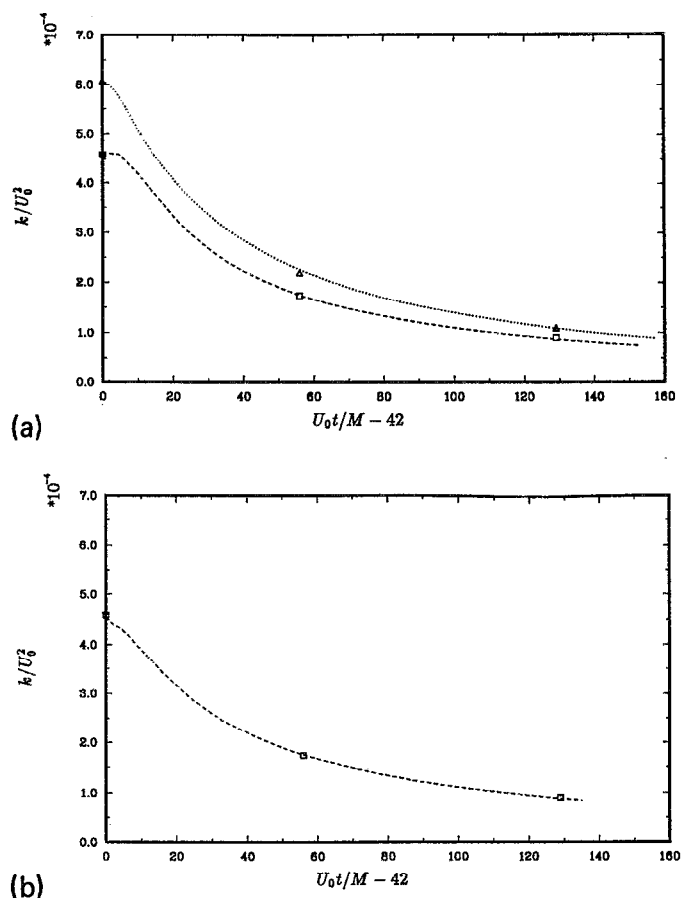


FIG. 7. (a) Time development of resolved-scale turbulence kinetic energy from LES of isotropic turbulence. \square , filtered data of Comte-Bellot and Corrsin¹⁰ (32^3); ---, LES (32^3 , $\alpha = 2$); Δ , filtered data of Comte-Bellot and Corrsin (64^3); ····, LES (64^3). (b) Effect of α on resolved-scale turbulence kinetic energy. \square , filtered data of Comte-Bellot and Corrsin (32^3); ---, LES (32^3 , $\alpha = 8/3$).

the accuracy of the model. The solenoidal initial velocity field for the simulations had the same three-dimensional energy spectrum as in the (high Reynolds number) experiment¹⁰ at the first station downstream of the turbulence-generating grid in the wind tunnel ($tU_0/M = 42$, where tU_0 is the downstream distance, U_0 is mean flow velocity, and M is the mesh size). The dilatational turbulence kinetic energy was zero initially and remained small throughout the simulations. Extensive experimental data were provided at three downstream locations, $tU_0/M = 42, 98$, and 171. The microscale Reynolds number in the experiments was 72 at the first station, and decreased to 60 at the last station, $tU_0/M = 171$. In the same distance, the rms streamwise turbulence intensity decayed by more than a factor of 2. The initial pressure fields were obtained from the solution of the incompressible Poisson equation. To further assess the robustness of the model, two grid resolutions, 32^3 and 64^3 , were used for the large eddy simulations. The corresponding turbulence Mach numbers M_t in the initial fields were 0.30 for the 32^3 grid and 0.35 for the 64^3 grid. The decay of the resolved turbulence kinetic energy is compared with the *filtered* experimental data at the two subsequent measurement stations ($tU_0/M = 98$ and 171) in Fig. 7(a). The agreement

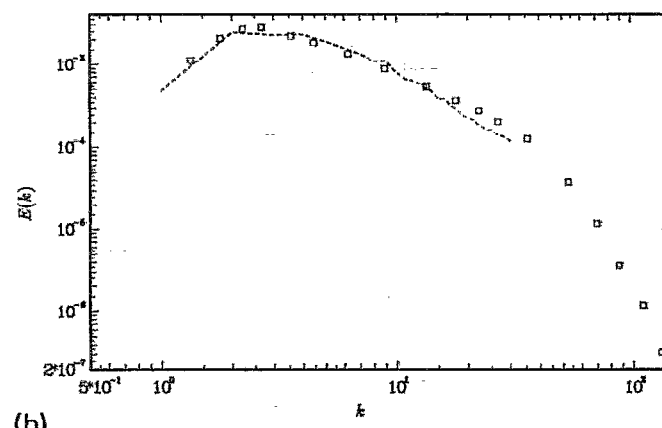
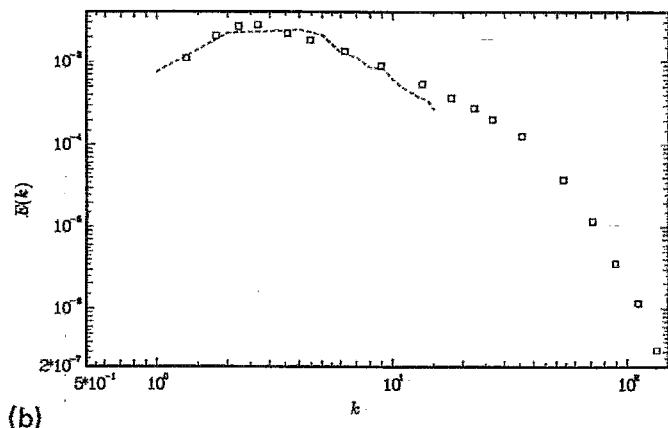
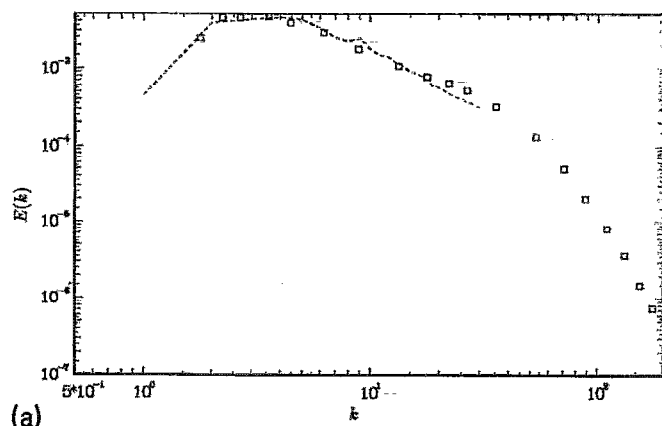
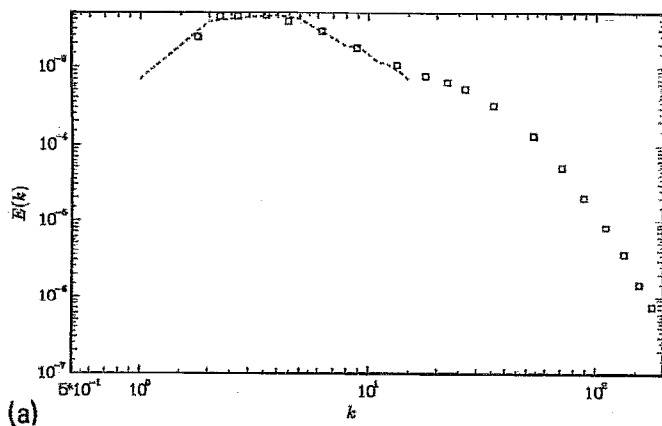


FIG. 8. Comparison of radial energy spectrum to data of Comte-Bellot and Corrsin. \square , experiment; ----, LES result (32^3). (a) $U_0 t/M = 98$. (b) $U_0 t/M = 171$.

FIG. 9. Comparison of radial energy spectrum to data of Comte-Bellot and Corrsin. \square , experiment; ----, LES result (64^3). (a) $U_0 t/M = 98$. (b) $U_0 t/M = 171$.

is excellent for both computational grid resolutions. This is a remarkable prediction because it did not involve any adjustable constants; the same model used for the transitional and turbulent channel flow accurately predicted the decay of isotropic turbulence. The evolution of turbulent kinetic energy for a LES with $\alpha = 8/3$ is shown in Fig. 7(b). The results demonstrate insensitivity to α , which is the only adjustable parameter in the SGS model. All subsequent results were obtained with $\alpha = 2$. The computed and experimental three-dimensional energy spectra are compared in Figs. 8 and 9. Again, good agreement is evident. An estimate of total turbulent kinetic energy can be made using Eq. (10) for the SGS kinetic energy; when added to the resolved turbulence kinetic energy, the result is within 5% of the total turbulent kinetic energy reported in Ref. 10 at the two downstream locations.

The model coefficients from both 32^3 and 64^3 LES computations are shown in Fig. 10. As in the *a priori* tests the model coefficients are higher in the coarse LES, but, in contrast to the *a priori* tests, C_I is larger than C in both simulations. It is interesting to note that the equilibrium value of C shown in Fig. 10 is comparable to the value of the Smagorinsky constant used in early LES studies of isotropic turbulence.⁹ Another result that illustrates departure from *a priori* tests is that in the LES the magnitude of the gradient of

the SGS kinetic energy was comparable to (40%–50% of) the magnitude of the thermodynamic pressure gradient. Although *a priori* tests are useful in the evaluation of SGS turbulence models, these and similar results obtained in turbulent channel flow⁶ reveal their limitation in extrapolating the performance of the actual LES calculations. In the present study, large eddy simulations performed at the same Reynolds number as in the DNS computations appear to be consistent with the *a priori* test results. For example, in computations at $Re_\lambda = 50$, the magnitude of the SGS kinetic energy gradient is small (less than 5%) relative to the thermodynamic pressure gradient, consistent with the *a priori* test results discussed in Sec. III A [see also Fig. 1(b)].

To demonstrate the role of the SGS model in obtaining the results in Figs. 7–9, we performed a DNS of the Comte-Bellot and Corrsin¹⁰ experiment with a resolution of 32^3 . The three-dimensional energy spectrum at $tU_0/M = 95$ is shown in Fig. 11. It is clear that excessive pileup of energy at the small scales results. In fact, computations became unstable before $tU_0/M = 98$ was reached. This result is to be expected since in the corresponding LES the magnitude of SGS dissipation was an order of magnitude larger than viscous dissipation.

The one-dimensional (1-D) longitudinal energy spectrum from the 32^3 LES is compared with the filtered experi-

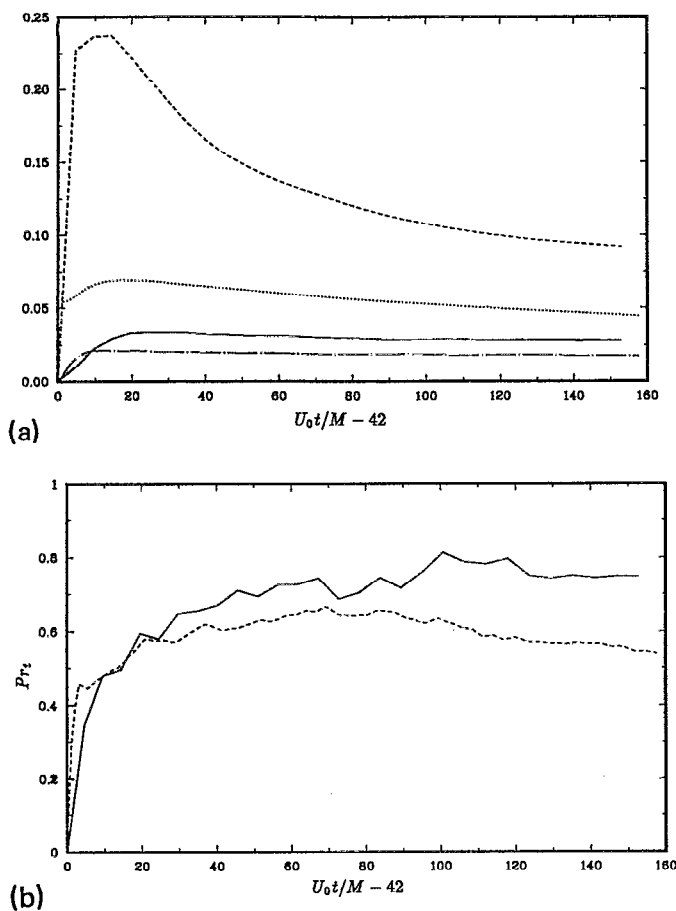


FIG. 10. (a) Time development of model coefficients from LES of isotropic turbulence. —, C (32^3); ---, C_t (32^3); -·-, C (64^3); ···, C_t (64^3). (b) Time development of turbulent Prandtl number from LES of isotropic turbulence. — (32^3); --- (64^3).

mental measurements¹⁰ in Fig. 12(a). The overall agreement is good. However, some energy pileup is evident near the cutoff. The excess energy at the small scales was found to be due to aliasing errors. Partial removal of aliasing errors (by zero-padding Fourier coefficients before calculating the

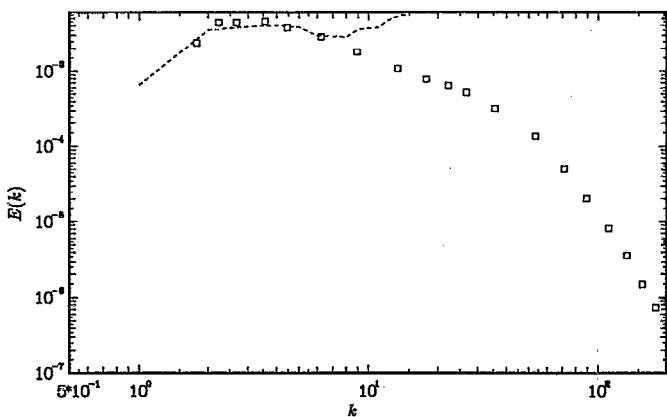
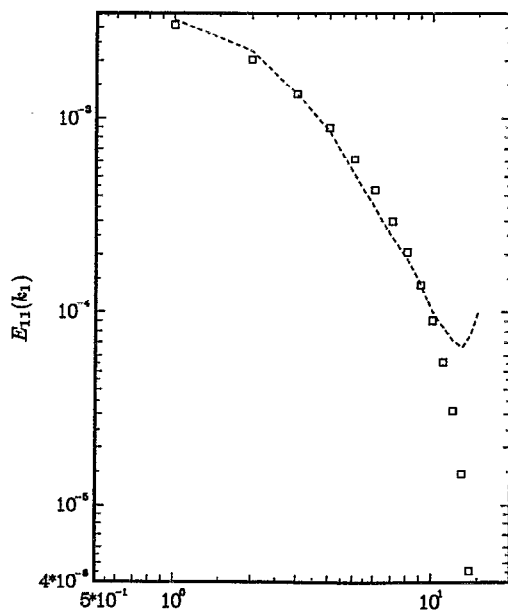
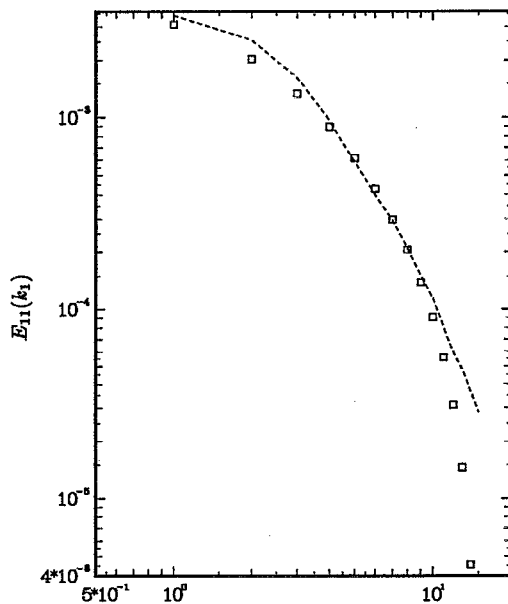


FIG. 11. Radial energy spectrum from DNS of isotropic turbulence. \square , experimental data of Comte-Bellot and Corrsin at $U_0 t / M = 98$; ---, DNS result at $U_0 t / M = 95$ (32^3).



(a)



(b)

FIG. 12. Comparison of one-dimensional energy spectrum to data of Comte-Bellot and Corrsin at $U_0 t / M = 98$. \square , experiment; ---, LES result. (a) 32^3 ; (b) 64^3 , truncated at $k_t = 32$.

products in the nonlinear terms) led to the improved energy spectrum shown in Fig. 12(b). Note that complete removal of aliasing errors in compressible flow calculations is especially difficult due to the presence of divisions. From examination of three-dimensional (3-D) spectra, Erlebacher *et al.*⁸ concluded that aliasing errors were not significant. Three-dimensional energy spectra from the present study (Figs. 8 and 9) also do not show any evidence of aliasing errors. The turbulence kinetic energy in the computational

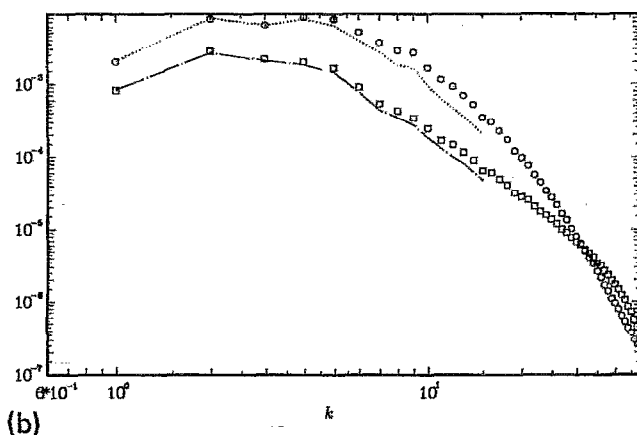
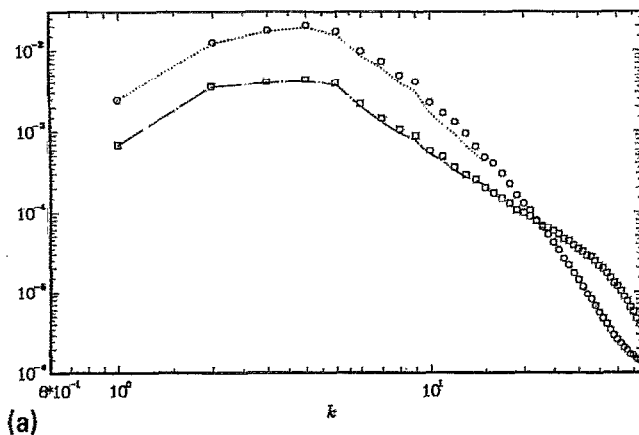


FIG. 13. Radial energy spectrum from compressible turbulence. (a) $t/\tau_t = 0.72$; (b) $t/\tau_t = 1.98$. \square , dilatational velocity (DNS, 96^3); \circ , solenoidal velocity (DNS, 96^3); ---, dilatational velocity (LES, 32^3); ····, solenoidal velocity (LES, 32^3).

box is also unaffected by the aliasing errors. Apparently, however, the 1-D energy spectrum is more sensitive to aliasing errors.

B. Compressible simulations

Experimental data for compressible isotropic turbulence are not available. Therefore, DNS results computed using a 96^3 mesh were used to test the accuracy of the large eddy simulation. For the simulations of compressible turbulence the initial 3-D energy spectrum of the solenoidal and dilatational velocity components was the same as in Sec. III A. The energy spectrum was scaled such that the initial fluctuation Mach number, M_t , was equal to 0.4. The fraction of kinetic energy initially contained in the dilatational velocity field was 20% of the total. The density field was initially uniform and the initial pressure fluctuations were scaled such that the compressible energy was equally partitioned between the kinetic and potential modes. Thus, these simulations provide a good test of the dynamic model for flows in which the dilatational component of the velocity is not negligible and thermal pressure fluctuations are relatively large.

The large eddy simulations were computed using 32^3 grid points and the initial 3-D energy spectrum was the same as the DNS spectrum up to the cutoff wave number. Shown in Figs. 13(a) and 13(b) are the energy spectra of the sole-

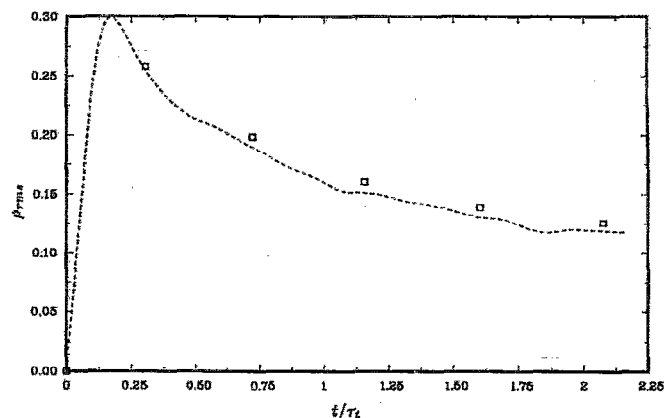


FIG. 14. Time development of rms density fluctuations from compressible turbulence. \square , filtered DNS, 96^3 ; ---, LES, 32^3 .

noidal and dilatational velocity components at two instances in the flow evolution. The results in Fig. 13(a) correspond to a time in which the total kinetic energy had decayed 30% from its initial value (0.72 eddy turnover times). From this figure it is evident that significant SGS energy is contained in the dilatational component of the velocity. There is good agreement between the LES and DNS spectra. The spectra in Fig. 13(b) are from the final time of the simulation at which the total kinetic energy had decayed 65% from its initial value (1.98 eddy turnover times). This figure shows that the spectrum of the dilatational velocity component is well predicted by the LES while the solenoidal velocity from the LES shows greater dissipation at the high wave numbers than that from the DNS.

The evolution of the rms density fluctuations from the LES is compared to the (filtered) DNS fluctuations in Fig. 14. The agreement between the LES and DNS results is good. This again demonstrates that the dynamic model is able to provide good descriptions of highly compressible turbulence. The equilibrium values of the model coefficients, C , C_r , and Pr_t , for this case were 0.0125, 0.0175, and 0.4, respectively. Finally, it should be emphasized that DNS with the LES grid (32^3) led to an excessive buildup of energy near the cutoff wave number, similar to that observed in Fig. 11.

In order to assess the performance of the dynamic model at higher Reynolds numbers, we performed two large eddy simulations at $Re_\lambda = 250$ (for which there is no comparable DNS data): one with fixed model constants corresponding to those used by Erlebacher *et al.*⁸ ($C = 0.0085$ and $C_r = 0$), and one with the dynamic model. The LES with fixed model constants experienced excessive accumulation of energy at high wave numbers, while the LES with the dynamic model did not. These calculations clearly show the need for dynamic SGS models that can adjust to flow conditions at different Reynolds numbers and Mach numbers.

V. CONCLUSIONS

A dynamic subgrid-scale model for compressible flows and the energy equation was developed. The model coeffi-

cients are computed instantaneously as a function of the flow variables. The dynamic subgrid-scale model coefficients and turbulent Prandtl number were computed using direct numerical simulation data from isotropic turbulence, homogeneous shear flow, and turbulent channel flow. The dependence of the subgrid-scale turbulent Prandtl number on the flow and scalar parameters were in accordance with the direct numerical simulation data for the total turbulent Prandtl number. Excellent agreement was obtained between the large eddy simulation results using the dynamic model and the experimental and direct numerical simulation data.

ACKNOWLEDGMENT

This work was supported in part by AFOSR Grant No. AFOSR-88-NA-0249.

¹J. Smagorinsky, Mon. Weather Rev. **91**, 99 (1963).

²J. W. Deardorff, J. Fluids Eng. **95**, 429 (1973).

³U. Schumann, J. Comput. Phys. **18**, 376 (1975).

⁴J. Bardina, J. H. Ferziger, and W. C. Reynolds, AIAA Paper No. 80-1357, 1980.

⁵M. Lesieur, *Turbulence in Fluids* (Martinus Nijhoff, Dordrecht, The Netherlands, 1987).

⁶M. Germano, U. Piomelli, P. Moin, and W. H. Cabot, Phys. Fluids A **3**, 1760 (1991). Corrigendum to appear in Phys. Fluids A.

⁷M. Germano, Center for Turbulence Research Manuscript 116, Stanford University and NASA-Ames Research Center, 1990.

⁸G. Erlebacher, M. Y. Hussaini, C. G. Speziale, and T. A. Zang, ICASE Report 90-76, ICASE/NASA Langley Research Center, 1990.

⁹N. N. Mansour, P. Moin, J. H. Ferziger, and W. C. Reynolds, in *Turbulent Shear Flows I*, edited by F. Durst, B. E. Launder, F. W. Schmidt, and J. H. Whitelaw (Springer-Verlag, Berlin, 1979), pp. 386-401.

¹⁰G. Comte-Bellot and S. Corrsin, J. Fluid Mech. **48**, 273 (1971).

¹¹A. Yoshizawa, Phys. Fluids **29**, 2152 (1986).

¹²S. Lee, P. Moin, and S. K. Lele, Phys. Fluids A **3**, 657 (1991).

¹³T. M. Eidson, J. Fluid Mech. **158**, 245 (1985).

¹⁴M. Rogers, P. Moin, and W. C. Reynolds, Stanford University, Department of Mechanical Engineering, Report No. TF-25, 1986.

¹⁵J. Kim, P. Moin, and R. Moser, J. Fluid Mech. **177**, 133 (1987).

¹⁶J. Kim and P. Moin, in *Turbulent Shear Flows 6*, edited by J.-C. André, J. Cousteix, F. Durst, B. E. Launder, F. W. Schmidt, and J. H. Whitelaw (Springer-Verlag, Berlin, 1989), pp. 86-96.